Effective Surface Termination with Au on PtCo@Pt Core-Shell Nanoparticle: Microstructural Investigations and Oxygen Reduction Reaction Properties

doi: 10.1016/j.jelechem.2019.04.053

Effective Surface Termination with Au on PtCo@Pt Core-Shell Nanoparticle: Microstructural Investigations and Oxygen Reduction Reaction Properties

Shuntaro Takahashi[1], Naoto Todoroki[1*], Rikiya Myochi[1], Tetsuro Nagao[1], Noboru Taguchi[2], Tsutomu Ioroi[2], Felix E. Feiten[3], Yuki Wakisaka[3], Kiyotaka Asakura[3], Oki Sekizawa[4,5], Tomohiro Sakata[5], Kotaro Higashi[5], Tomoya Uruga[4,5], Yasuhiro Iwasawa[5], and Toshimasa Wadayama[1]

[1]Graduate School of Environmental Studies, Tohoku University, Sendai 980-8579, Japan

[2]Research Institute of Electrochemical Energy, National Institute of Advanced Industrial Science and Technology (AIST), Osaka 563-8577, Japan

[3]Institute for Catalysis (ICAT), Hokkaido University, Sapporo 001-0021, Japan

[4]Japan Synchrotron Radiation Research Institute (JASRI), Hyogo 679-5148, Japan

[5]Innovation Research Center for Fuel Cells, The University of Electro-Communications, Tokyo 182-8585, Japan

Keywords Oxygen reduction reaction, Pt–Co alloy, surface Au termination, core-shell nanoparticles, arc-plasma deposition

ABSTRACT

We investigated the microstructures of Au-deposited PtCo@Pt core-shell nanoparticles (NPs) and discussed enhancement of the oxygen reduction reaction (ORR) properties by Au termination of low-coordination sites of the Pt-shell. The Au-deposited PtCo@Pt NPs showed an improved electrochemical structural stability, together with slight increment in increased initial, pristine area-specific activity relative to the non-Au-deposited PtCo@Pt NPs. Atomic-level microstructural characterization was performed by a back-side illumination fluorescence X-ray absorption fine structure (BI-FXAFS) method and scanning transmission electron microscopy with energy dispersive spectroscopy (STEM-EDS). The BI-FXAFS results indicated that compressive lattice strain in the Pt-shells of the PtCo@Pt NPs was almost unchanged by the subsequent Au deposition. Furthermore, STEM-EDS mapping of Pt, Co, and Au clearly showed that the deposited Au tended to localize at low-coordination sites of the Pt-shell surface, e.g., edges and corners. The atomic-level microstructural characterization conducted in this study demonstrated that effective Au surface terminations of the Pt-shell enhances the ORR durability of Pt-based core-shell type NP catalysts.

1. Introduction

Developing highly active electrocatalysts for alternative energy devices, such as fuel cells and/or metal-air batteries, is urgently required to establish a future zero-carbon society [1]. The oxygen reduction reaction (ORR) is a key electrocatalytic process because it determines the overall reaction rate of a polymer electrolyte fuel cell (PEFC). Currently, Pt and Pt-based alloy nanoparticles (NPs) supported on carbon black are used as ORR electrocatalysts for PEFCs mounted on fuel cell vehicles (FCVs) [2]. However, further technological developments are needed to reduce Pt use to commercialize FCVs. Among various Pt and Pt-based alloy (Pt-M; M = 3d-transition metals, including Fe, Ni, and Co) catalysts [3-8], chemically or electrochemically dealloyed Pt-M NPs form core-shell nanostructures (Pt-M@Pt) and show enhanced ORR activity compared with pure Pt NPs [9, 10]. The initial, pristine ORR activity and electrochemical stability of the Pt-M@Pt NPs strongly depends on the atomic-level microstructures of the core-shell NPs, such as their particle shapes (surface atomic arrangements) [11-15], alloy compositions [7, 9, 16-18], and Pt-shell layer thicknesses [19-21]. Furthermore, as regards their durability, dissolution of the less-noble atoms M in strong acid electrolytes [22] under PEFC operating conditions (low pH, electrochemical potential fluctuations) strongly deactivates the core-shell catalysts.

Concerning the aforementioned background, various approaches for enhancing not only the ORR activity but also the durability of practical catalysts have been explored to overcome the disadvantages of core-shell type NP catalysts: atomic-level architectures of NP structures are proposed. For example, alloy NPs with ordered phases, such as $L1_0$-PtFe [23, 24] and $L1_0$-PtCo [25, 26], showed enhanced activity and durability. Another approach to improving the durability involves carbon-shell coating of Pt and Pt-based alloy NPs [27, 28]. Appropriate doping of different elements in pure Pt and Pt-based core-shell NPs is also effective in enhancing the durability of the NPs [29-32]. Especially, although Au is also expensive, appropriate Au doping in Pt-based alloy NPs have attractive attentions to improve the electrochemical stability [33, 34]. Indeed, we showed durability enhancement of Pt NPs by Au surface modification via suppression of NP agglomeration under the accelerated durability test (ADT) protocol [35]. In the aforementioned published papers, microstructural investigations were performed by conventional scanning transmission electron microscopy with energy dispersive spectroscopy (STEM-EDS), transmission X-ray absorption fine structure analysis (XAFS), and theoretical calculations. However, due to the low resolution of the structural analysis conducted, the atomic-level microstructures of core-shell type NPs should be further clarified experimentally. For example, for our model catalysts of Au-deposited Pt

and core-shell PtCo@Pt NPs synthesized by a dry process [35], the deposited amounts of Pt, Co, and Au, i.e., metal-loadings on a highly oriented pyrolytic graphite (HOPG) substrate used as a support, are insufficient to analyze via transmission XAFS [36], Furthermore, atomic-level separation of small amounts of Au from Pt using EDS is generally difficult at sub-nanometer levels, because the energies of the Lα lines of Pt (9.4 keV) and Au (9.7 keV) usually overlap. Therefore, more sensitive and high-resolution microstructural characterization methods for Au-deposited PtCo@Pt core-shell NPs should be used to determine the role of the Au on the ORR durability of practical Pt-shell/Pt-M alloy-core type catalysts.

In this study, we investigated the effect of Au surface modification of PtCo@Pt core-shell NPs on the ORR properties (activity and durability) by using a back-illuminated fluorescence XAFS (BI-FXAFS) method and high-resolution STEM-EDS. The results obtained clearly show that the surface Au localizes at low-coordination sites, e.g., the edges and/or corners of the PtCo@Pt core-shell NPs and thus improves the electrochemical stability (durability) under the ADT.

2. Experimental

2.1 Sample preparation

Two arc plasma deposition (APD) sources (ULVAC-RIKO ARL-300) were used

to synthesize the PtCo alloy NPs under a N_2 partial pressure of 0.1 Pa on HOPG substrates (10 mm × 10 mm; thickness: 1 mm, Optigraph). We previously reported that N_2-treated alloy NPs form a PtCo@Pt core-shell structure after electrochemical dealloying [37]. The Au-PtCo@Pt was prepared by APD of Au on the as-deposited PtCo NPs, and the electrochemical dealloying was then performed under the conditions described in the following electrochemical measurements section. The substrate HOPG temperature during the APD (Pt, Co, and Au) was maintained at 773 K. The total deposited amounts of Pt, Co, and Au are estimated with a quartz crystal microbalance installed in the APD chamber and normalized to the HOPG geometric surface area to calculate the surface densities for the NPs: the estimated densities are 0.57 μg cm^{-2} (Pt), 0.34 μg cm^{-2} (Co), and 0.076 μg cm^{-2} (Au). The alloy compositions of as-deposited PtCo NPs with and without NPs are summarized in Table S2.

2.2 Electrochemical measurements

The APD-prepared PtCo@Pt and Au-PtCo@Pt NP samples were transferred from the APD chamber to an electrochemical measurement setup in a N_2-purged glove box without exposure to air [35], A potentiostat combined with a rotating disk electrode (RDE) system (HZ-5000, Hokuto Denko) was used, and electrochemical experiments

were conducted with a glass cell containing a Pt counter electrode and a reversible hydrogen electrode (RHE) with flowing H_2 gas. The electrolyte solution was prepared from perchloric acid ($HClO_4$; Ultrapure, Kanto Chemical) and Milli-Q water. The APD-prepared NP samples were electrochemically dealloyed by applying PCs between 0.05 and 1.05 V for 300 cycles at 500 mV s^{-1} in N_2-purged 0.1 M $HClO_4$. Cyclic voltammetry (CV) and linear sweep voltammetry (LSV) for the samples were conducted in N_2-purged (scan rate of 50 mV s^{-1} without disk rotation) and O_2-saturated 0.1 M $HClO_4$ (10 mV s^{-1} with disk rotation rates of 400–2,500 rpm). The electrochemical surface area of Pt ($ECSA_{Pt}$) was estimated from the hydrogen adsorption charge in the potential region from 0.08 to 0.38 V, assuming that the charge for the monolayer hydrogen adsorption [38] was 210 μC cm^{-2}. We used Koutecky–Levich plots to estimate the kinetically controlled currents (i_k) at 0.9 V vs. RHE. Mass activities and area-specific activities of the prepared samples were estimated using equations (1) and (2), respectively.

$$Mass\ Activity\ (A/mg_{-Pt}) = i_k(mA)/deposited\ Pt\ mass\ (\mu g) \quad (1)$$

$$Area\ Specific\ Activity\ (mA/cm^2_{-ECS}\ ) = i_k\ (mA)/ECSA_{Pt}\ (cm^2) \quad (2)$$

The electrochemical stabilities of the PtCo@Pt and Au-PtCo@Pt core-shell NP samples were estimated by applying potential cycles (PCs) of square waves between 0.6 and 1.0 V (3 s each) in an O_2-saturated, room temperature electrolyte. All the EC measurements

were conducted at least three times for the same sample to be evaluated.

2.3 Microstructural characterization

The morphologies of the dealloyed PtCo NPs with and without APD of Au were observed using scanning tunneling microscopy (STM; Bruker MultiMode V) in air. The NP distributions were estimated from the corresponding STM images using ImageJ analysis software. BI-FXAFS [39] measurements were performed on the electrochemically dealloyed NPs in N_2-purged 0.1 M $HClO_4$ at 0.4 V vs. RHE by using a home-made BI-FXAFS electrochemical cell at the beamline of SPring-8 (BL36XU) in Japan. The electrode potential in double layer region (0.4 V) and inert atmosphere of the solution were selected to avoid micro structural changes by surface adsorbed species and, then, dissolution of oxygen in air into the solution should occur during the XAFS measurements. XAFS data analysis was conducted with the Hephaestus software package [40]. The detailed analysis method is described in the Supporting Information. Atomic-level microstructural analysis was performed for the dealloyed NPs prepared on an amorphous carbon thin film by using STEM (FEI Titan3 G2 60-300) equipped with a Super-X EDS system.

3. Results and discussion

Fig. 1 shows scanning tunneling microscopic (STM) images (left) and corresponding particle size distributions (right) for PtCo@Pt (a) and Au-PtCo@Pt NPs (b). It can be seen that spherical NPs are distributed on the HOPG substrates after electrochemical dealloying of the arc-plasma deposited Pt, Co, and Au. The STM images for both samples indicate that their average diameters are similar, suggesting that the distributions of the prepared NPs are almost independent of the subsequent APD of Au.

Electrochemical measurements were performed after electrochemical dealloying (conditions are described in the Experimental section). Cyclic voltammograms (CVs) of the PtCo@Pt and Au-PtCo@Pt NP samples recorded in N_2-purged 0.1 M $HClO_4$ are shown in Fig. 2(a). In the hydrogen-related region (0.05–0.35 V), redox peaks around 0.19 V due to hydrogen adsorption and desorption ($H_{ads\&des}$) on the Pt-shell surfaces decreased for the Au-PtCo@Pt NP sample in comparison to those for the non-Au-deposited PtCo@Pt. The redox peaks can be ascribed to $H_{ads\&des}$ reactions on low-coordination sites of the Pt-shell surface, such as edges and corners [41]. Considering that $H_{ads\&des}$ reactions hardly occur on the Au surface in the potential region from 0.05–0.35 V [42], the CV results suggest that the low-coordination sites of the Pt-shell could be preferentially terminated by subsequent APD of Au, even in the EC environment [35]. On

the other hand, adsorption charge of the oxygen-related species (OH, O) for the Au-PtCo@Pt significantly decreased in compared with that of the hydrogen (Table. S1). The difference in adsorption charges can stem from part of Au atoms also locate on the (111) and (100) terrace sites as surface alloys or nano-islands. The detailed analysis for the adsorption charges are indicated in Supporting Information. The initial, pristine mass activity and area-specific activity for ORR at 0.9 V were estimated from the results of the polarization curves (Fig. S8(a)) and the results are summerized in Fig. 2(b). Recently reported ORR activities of commercial Pt/C [10, 43] are also added to the Figure. The PtCo@Pt and Au-PtCo@Pt showed ca. 7- and 5-times higher mass activity than typical commercial Pt/C. The decrease in the mass activity of Au-PtCo@Pt relative to PtCo@Pt can be explained by a decrease in the electrochemical surface area of Pt ($ECSA_{Pt}$) with the subsequent APD of Au. Conversely, the initial, area-specific activity of the Au-PtCo@Pt sample was slight higher than that of PtCo@Pt. A similar activity enhancement by subsequent Au deposition was also shown in Au/Pt NP systems [35], which was probably caused by inhomogeneous distribution of the deposited Au on the Pt-shell surface. These results will be discussed later.

Mass activity changes in the dealloyed NPs during the ADT PCs are shown in Fig. 3(a). Changes in CVs before and after the ADT are depicted in Fig. S2. Also, the

polarization curves for the samples recorded during the ADT are summarized in Fig. S7. The mass activity for the non-Au-deposited PtCo@Pt NPs monotonically decreased as the number of PCs increased. After 10,000 cycles, the activity was about half of the initial value. Conversely, for the Au-PtCo@Pt NPs, the activity increased slightly up to 1,000 PCs and then decreased slightly: the activity after 10,000 PCs for Au-PtCo@Pt was 14% higher than that of the non-Au-deposited PtCo@Pt NPs. As shown in the STM images in Fig. 3(b), the average particle sizes of PtCo@Pt increased from 4.5 to 5.7 nm when applying 10,000 PCs (ca. +25%), whereas the Au-deposited sample showed suppression of NP agglomeration (ca. +17%). The results show electrochemical stability enhancement of the PtCo@Pt NPs as a result of subsequent APD of Au.

To investigate the correlation between the ORR properties and the atomic structures of the PtCo@Pt NPs with and without Au, BI-FXAFS measurements were conducted in N_2-purged 0.1 M $HClO_4$ at 0.4 V vs. RHE. The structural parameters determined by extended X-ray absorption fine structure (EXAFS) curve-fitting analysis in combination with model building for the Au-PtCo@Pt, PtCo@Pt, and pure Pt NP samples are summarized in Table 1. EXAFS spectra and additional details of the EXAFS analysis are presented in Fig. S1 and in the Supporting Information, respectively. The incorporation of Co leads to a reduction in the number of Pt nearest neighbors, *N(Pt-Pt)*,

around Pt. Furthermore, respective values for the Pt-Pt distance, *R(Pt-Pt)*, in PtCo@Pt and Au-PtCo@Pt NPs are ca. 0.3% smaller than in the Pt NPs. Considering that the lattice parameters of PtCo alloys are generally smaller than those of pure Pt (for example, Pt: 0.393 nm, Pt_3Co: 0.385 nm) [44], a decrease in *the Pt-Pt bond length* suggests that compressive surface strain should work on the Pt-shell, irrespective of the subsequent APD of Au. Accordingly, compressive strains of the Pt-shell, not only for PtCo@Pt but also for Au-PtCo@Pt, should enhance the ORR activity [45, 46]. The BI-FXAFS measurements conducted under the EC conditions (N_2-purged 0.1 M $HClO_4$ at 0.4 V vs. RHE) clearly show the effect of the subsequent APD of Au on the electrochemical ORR that proceeds on the core-shell NPs.

The atomic-level inhomogeneous distribution of Au on the PtCo@Pt NPs was discussed based on high-resolution STEM and EDS mapping of the Au-PtCo@Pt NP sample: the results are summarized in Fig. 4. The high-angle annular dark-field (HAADF)-STEM images (Fig. 4(a) and (b)) show clear lattice fringes and Z-contrast induced by the atomic number difference between Pt (Z = 78) and Co (Z = 27). Especially, as shown in magnified image (b), the center of the NP is darker than the surface. The observed image clearly indicates that Co is enriched in the core of the PtCo@Pt NP. The STEM-EDS mapping of the Au-PtCo@Pt sample is summarized in Fig. 4(c). The image

smoothing procedure is described in Fig. S3 in the Supporting Information. The maps of Pt (red) and Co (blue) clearly show that the NPs form PtCo-alloy-core@Pt-shell core-shell structures. Judging from the image of "Pt+Co", the Pt-shell thickness can be estimated as ca. 1 nm (3~4 atomic layers of Pt), and this is consistent with the non-Au-deposited PtCo@Pt [37]. The results reveal that the subsequent Au deposition does not significantly affect the individual PtCo@Pt core-shell structure. As regards the Au distribution on the PtCo@Pt NPs, the magnified map (Fig. 4(d); left) of Pt and Au (green) exhibits inhomogeneous, mottled Au distributions on the core-shell NP surface, where a yellow region stemming from overlap of Pt and Au atoms (yellow; "Pt+Au") appears at the circumference of the terrace parts of the Pt-shell (red; "Pt"). The corresponding STEM-EDS spectra (Fig. 4(d); right) for the square-enclosed areas of the left image of Fig. 4(d) strongly support Au localization on the surface of the NP (See also Fig. S5). Although the characteristic X-ray component due to Au (Lα 9.7 keV) is absent in the energy spectrum of Area 1, this component appears in the spectrum of Area 2. Furthermore, close inspection of the image shows green regions ("Au") around the particle surface adjacent to the yellow region located at the circumference of the terrace part of the Pt-shell. Therefore, the HAADF-STEM and corresponding EDS (Fig. 4) results indicate that the deposited Au is enriched on the surface of PtCo@Pt NPs, especially at

the edges and/or corners of the Pt-shell, as shown in the cuboctahedral NP model in Fig. 4(e). The ORR activity for the terraced site with an atomic arrangement of (111) is higher than at the edge or corner sites [47]. Jinnouchi et al. showed by DFT calculations that the edge sites of pure Pt NPs are well covered with oxygen-containing adsorbates at 0.9 V and are therefore inactive for the ORR [32]. Considering the aforementioned discussion, the effective Au termination of edges and/or corners probably resulted in area-specific activity enhancement of the pristine Au-PtCo@Pt NPs (Fig. 2(b)).

We investigated Au-induced ORR durability changes for the APD-Pt NPs and deduced that surface Au can block Pt-dissolution that preferentially starts from the low-coordination sites of the NPs (edges and corners) [35]. For PtCo@Pt and Au-PtCo@Pt, degradation of the NPs probably begins with surface rearrangement following dissolution of Pt under the oxidation-reduction PCs (ADT). Such behavior of the surface Pt atoms should preferentially occur at the low-coordination sites of the Pt-shell surface [48]. Consequently, as the number of PCs increases, less-noble Co atoms in the PtCo-core could react with the strong acid electrolyte, resulting in significant dissolution of Co. The mass activity of the PtCo@Pt NP sample decreased as the number of PCs increased (Fig. 3(a) red), corresponding to Co dissolution during the ADT. Conversely, the degradation slope of the Au-PtCo@Pt NP sample (blue) is gentle in comparison to that of PtCo@Pt,

and after 10,000 PCs, the estimated average size of the former Au-PtCo@Pt NP is smaller than that of latter PtCo@Pt, as shown in the STM images (Fig. 3 (b)). Accordingly, we deduce that the effective termination of the low-coordination sites (edges and/or corners) by APD of Au suppresses the electrochemical structural degradation of the core-shell NPs. The results indicate that this atomic-level catalyst design is suitable for developing electrochemically stable core-shell NP type catalysts.

4. Conclusions

We investigated the ORR properties (activity and durability) of Au-terminated PtCo@Pt core-shell NPs (Au-PtCo@Pt) prepared by APD of Pt, Co, and Au and discussed the ORR properties of Au-PtCo@Pt based on BI-FXAFS and STEM-EDS results. The Au-PtCo@Pt NP sample showed enhanced electrochemical structural stability under ADT compared with the non-Au-deposited PtCo@Pt NP sample. The average size of the PtCo@Pt NPs estimated by STM was nearly unchanged by the subsequent APD of Au and the BI-FXAFS results showed that the average Pt-Pt bond distance *R* of the Au-PtCo@Pt NP sample was almost unaffected by the APD of Au. Furthermore, the STEM-EDS results showed that the post-deposited Au tend to localize at or near edge and corner sites of the Pt-shell of the core-shell NPs. Based on the obtained results, we conclude that surface terminations of the low-coordination sites of the Pt-shell

by Au contribute substantially to the electrochemical stability enhancement of the core-shell NPs. The results obtained in this study offer a basic strategy for developing electrocatalysts through effective surface termination of highly active core-shell NPs by Au as an electrochemically stable element.

Acknowledgements

This study was supported by the New Energy and Industrial Technology Development Organization (NEDO) of Japan, a Grant-in-Aid for Challenging Exploratory Research from the Japan Society for the Promotion of Science (16K14397), and by the Cooperative Research Program of Institute for Catalysis, Hokkaido University (Grant #16B1024). Synchrotron radiation experiments were performed at the BL36XU beamline of SPring-8 with the approval of the Japan Synchrotron Radiation Research Institute (JASRI) (Proposal Nos. 2016B7905, 2017B7905).

Appendix A. Supplementary data

Supplementary material related to this article can be found, in the online version. The materials contain additional information including electrochemical results, the EXAFS measurements, and STEM-EDS observations, XPS analysis, ORR polarization curves.

Notes

The authors declare no competing financial interests.

References

[1] H.A. Gasteiger, N.M. Marković, Just a Dream—or Future Reality?, Science, 324 (2009) 48-49.

[2] I.E.L. Stephens, J. Rossmeisl, I. Chorkendorff, Toward sustainable fuel cells, Science, 354 (2016) 1378-1379.

[3] C. Zhang, X. Shen, Y. Pan, Z. Peng, A review of Pt-based electrocatalysts for oxygen reduction reaction, Front. Energy, 11 (2017) 268-285.

[4] Z.W. Seh, J. Kibsgaard, C.F. Dickens, I. Chorkendorff, J.K. Nørskov, T.F. Jaramillo, Combining theory and experiment in electrocatalysis: Insights into materials design, Science, 355 (2017) 1-12.

[5] T. Ioroi, K. Yasuda, Platinum-Iridium Alloys as Oxygen Reduction Electrocatalysts for Polymer Electrolyte Fuel Cells, J. Electrochem. Soc., 152 (2005) A1917-A1924.

[6] X. Zhao, S. Takao, K. Higashi, T. Kaneko, G. Samjeskè, O. Sekizawa, T. Sakata, Y. Yoshida, T. Uruga, Y. Iwasawa, Simultaneous Improvements in Performance and Durability of an Octahedral PtNix/C Electrocatalyst for Next-Generation Fuel Cells by Continuous, Compressive, and Concave Pt Skin Layers, ACS Catal., 7 (2017) 4642-4654.

[7] A. Kulkarni, S. Siahrostami, A. Patel, J.K. Norskov, Understanding Catalytic Activity Trends in the Oxygen Reduction Reaction, Chem. Rev., 118 (2018) 2302-2312.

[8] E. Antolini, The oxygen reduction on Pt-Ni and Pt-Ni-M catalysts for low-temperature

acidic fuel cells: A review, International Journal of Energy Research, 0 (2018).

[9] B. Han, C.E. Carlton, A. Kongkanand, R.S. Kukreja, B.R. Theobald, L. Gan, R. O'Malley, P. Strasser, F.T. Wagner, Y. Shao-Horn, Record activity and stability of dealloyed bimetallic catalysts for proton exchange membrane fuel cells, Energ. Environ. Sci., 8 (2015) 258-266.

[10] H. Kwon, M.K. Kabiraz, J. Park, A. Oh, H. Baik, S.-I. Choi, K. Lee, Dendrite-Embedded Platinum–Nickel Multiframes as Highly Active and Durable Electrocatalyst toward the Oxygen Reduction Reaction, Nano Lett., 18 (2018) 2930-2936.

[11] L. Gan, S. Rudi, C. Cui, M. Heggen, P. Strasser, Size-Controlled Synthesis of Sub-10 nm PtNi3 Alloy Nanoparticles and their Unusual Volcano-Shaped Size Effect on ORR Electrocatalysis, Small, 12 (2016) 3189-3196.

[12] Y. Kang, X. Ye, J. Chen, Y. Cai, R.E. Diaz, R.R. Adzic, E.A. Stach, C.B. Murray, Design of Pt–Pd Binary Superlattices Exploiting Shape Effects and Synergistic Effects for Oxygen Reduction Reactions, J. Am. Chem. Soc., 135 (2012) 42-45.

[13] S. Kobayashi, M. Wakisaka, D.A. Tryk, A. Iiyama, H. Uchida, Effect of Alloy Composition and Crystal Face of Pt-Skin/Pt100–xCox [(111), (100), and (110)] Single Crystal Electrodes on the Oxygen Reduction Reaction Activity, J. Phys. Chem. C, 121 (2017) 11234-11240.

[14] Y. Yamada, K. Miyamoto, T. Hayashi, Y. Iijima, N. Todoroki, T. Wadayama, Oxygen reduction reaction activities for Pt-enriched Co/Pt(111), Co/Pt(100), and Co/Pt(110) model catalyst surfaces prepared by molecular beam epitaxy, Surf. Sci., 607 (2013) 54-60.

[15] M. Liu, Z. Zhao, X. Duan, Y. Huang, Nanoscale Structure Design for High-Performance Pt-Based ORR Catalysts, Adv. Mater., 31 (2019) 1802234.

[16] L. Gan, M. Heggen, S. Rudi, P. Strasser, Core–Shell Compositional Fine Structures of Dealloyed PtxNi1–x Nanoparticles and Their Impact on Oxygen Reduction Catalysis, Nano Lett., 12 (2012) 5423-5430.

[17] Y.-J. Wang, N. Zhao, B. Fang, H. Li, X.T. Bi, H. Wang, Carbon-Supported Pt-Based Alloy Electrocatalysts for the Oxygen Reduction Reaction in Polymer Electrolyte Membrane Fuel Cells: Particle Size, Shape, and Composition Manipulation and Their Impact to Activity, Chem. Rev., 115 (2015) 3433-3467.

[18] N. Todoroki, R. Kawamura, M. Asano, R. Sasakawa, S. Takahashi, T. Wadayama, Alloy-composition-dependent oxygen reduction reaction activity and electrochemical stability of Pt-based bimetallic systems: a model electrocatalyst study of Pt/PtxNi100−x(111), Phys. Chem. Chem. Phys., 20 (2018) 11994-12004.

[19] N. Todoroki, Y. Asakimori, T. Wadayama, Effective shell layer thickness of platinum for oxygen reduction reaction alloy catalysts, Phys. Chem. Chem. Phys., 15 (2013) 17771-17774.

[20] C. Wang, M. Chi, D. Li, D. Strmcnik, D. van der Vliet, G. Wang, V. Komanicky, K.C. Chang, A.P. Paulikas, D. Tripkovic, J. Pearson, K.L. More, N.M. Markovic, V.R. Stamenkovic, Design and synthesis of bimetallic electrocatalyst with multilayered Pt-skin surfaces, J. Am. Chem. Soc., 133 (2011) 14396-14403.

[21] M. Shao, J.H. Odell, A. Peles, D. Su, The role of transition metals in the catalytic activity of Pt alloys: quantification of strain and ligand effects, Chem. Commun., 50 (2014) 2173-2176.

[22] H.A. Gasteiger, S.S. Kocha, B. Sompalli, F.T. Wagner, Activity benchmarks and requirements for Pt, Pt-alloy, and non-Pt oxygen reduction catalysts for PEMFCs, Appl. Catal., B, 56 (2005) 9-35.

[23] J. Li, Z. Xi, Y.-T. Pan, J.S. Spendelow, P.N. Duchesne, D. Su, Q. Li, C. Yu, Z. Yin, B. Shen, Y.S. Kim, P. Zhang, S. Sun, Fe Stabilization by Intermetallic L10-FePt and Pt Catalysis Enhancement in L10-FePt/Pt Nanoparticles for Efficient Oxygen Reduction Reaction in Fuel Cells, J. Am. Chem. Soc., 140 (2018) 2926-2932.

[24] Q. Li, L. Wu, G. Wu, D. Su, H. Lv, S. Zhang, W. Zhu, A. Casimir, H. Zhu, A. Mendoza-Garcia, S. Sun, New Approach to Fully Ordered fct-FePt Nanoparticles for Much Enhanced Electrocatalysis in Acid, Nano Lett., 15 (2015) 2468-2473.

[25] Q. Jia, K. Caldwell, D.E. Ramaker, J.M. Ziegelbauer, Z. Liu, Z. Yu, M. Trahan, S. Mukerjee, In Situ Spectroscopic Evidence for Ordered Core–Ultrathin Shell Pt1Co1 Nanoparticles with Enhanced Activity and Stability as Oxygen Reduction Electrocatalysts, J. Phys. Chem. C, 118 (2014) 20496-20503.

[26] W. Xiao, W. Lei, M. Gong, H.L. Xin, D. Wang, Recent Advances of Structurally Ordered Intermetallic Nanoparticles for Electrocatalysis, ACS Catal., (2018) 3237-3256.

[27] D.Y. Chung, S.W. Jun, G. Yoon, S.G. Kwon, D.Y. Shin, P. Seo, J.M. Yoo, H. Shin, Y.-H. Chung, H. Kim, B.S. Mun, K.-S. Lee, N.-S. Lee, S.J. Yoo, D.-H. Lim, K. Kang, Y.-E. Sung, T. Hyeon, Highly Durable and Active PtFe Nanocatalyst for Electrochemical Oxygen Reduction Reaction, J. Am. Chem. Soc., 137 (2015) 15478-15485.

[28] K. Cheng, Z. Kou, J. Zhang, M. Jiang, H. Wu, L. Hu, X. Yang, M. Pan, S. Mu, Ultrathin carbon layer stabilized metal catalysts towards oxygen reduction, J. Mater. Chem. A, 3 (2015) 14007-14014.

[29] M. Gatalo, P. Jovanovič, G. Polymeros, J.-P. Grote, A. Pavlišič, F. Ruiz- Zepeda, V.S. Šelih, M. Šala, S. Hočevar, M. Bele, K.J.J. Mayrhofer, N. Hodnik, M. Gaberšček, Positive Effect of Surface Doping with Au on the Stability of Pt-Based Electrocatalysts, ACS Catal., 6 (2016) 1630-1634.

[30] H. Liu, W. An, Y. Li, A.I. Frenkel, K. Sasaki, C. Koenigsmann, D. Su, R.M. Anderson, R.M. Crooks, R.R. Adzic, P. Liu, S.S. Wong, In Situ Probing of the Active Site Geometry of Ultrathin Nanowires for the Oxygen Reduction Reaction, J. Am. Chem. Soc., 137 (2015) 12597-12609.

[31] X. Huang, Z. Zhao, L. Cao, Y. Chen, E. Zhu, Z. Lin, M. Li, A. Yan, A. Zettl, Y.M. Wang, X. Duan, T. Mueller, Y. Huang, High-performance transition metal–doped Pt3Ni octahedra for oxygen reduction reaction, Science, 348 (2015) 1230-1234.

[32] R. Jinnouchi, K.K.T. Suzuki, Y. Morimoto, DFT calculations on electro-oxidations and dissolutions of Pt and Pt–Au nanoparticles, Catal. Today, 262 (2016) 100-109.

[33] J. Choi, J. Cho, C.-W. Roh, B.-S. Kim, M.S. Choi, H. Jeong, H.C. Ham, H. Lee, Au-doped PtCo/C catalyst preventing Co leaching for proton exchange membrane fuel cells, Appl. Catal., B, 247 (2019) 142-149.

[34] Y. He, Y.L. Wu, X.X. Zhu, J.N. Wang, Remarkable Improvement of the Catalytic Performance of PtFe Nanoparticles by Structural Ordering and Doping, ACS Appl. Mater., 11 (2019) 11527-11536.

[35] S. Takahashi, H. Chiba, T. Kato, S. Endo, T. Hayashi, N. Todoroki, T. Wadayama, Oxygen reduction reaction activity and structural stability of Pt-Au nanoparticles prepared by arc-plasma deposition, Phys. Chem. Chem. Phys., 17 (2015) 18638-18644.

[36] Y. Iwasawa, Asakura, Kiyotaka, Tada, Mizuki XAFS Techniques for Catalysts, Nanomaterials, and Surfaces, Springer Nature, 2017.

[37] S. Takahashi, N. Takahashi, N. Todoroki, T. Wadayama, Dealloying of Nitrogen-Introduced Pt–Co Alloy Nanoparticles: Preferential Core–Shell Formation with Enhanced Activity for Oxygen Reduction Reaction, ACS Omega, 1 (2016) 1247-1252.

[38] S. Trasatti, O.A. Petrii, Real surface area measurements in electrochemistry, Pure

Appl. Chem., 63 (1991) 711-734.

[39] H. Uehara, Y. Uemura, T. Ogawa, K. Kono, R. Ueno, Y. Niwa, H. Nitani, H. Abe, S. Takakusagi, M. Nomura, Y. Iwasawa, K. Asakura, In situ back-side illumination fluorescence XAFS (BI-FXAFS) studies on platinum nanoparticles deposited on a HOPG surface as a model fuel cell: a new approach to the Pt-HOPG electrode/electrolyte interface, Phys. Chem. Chem. Phys., 16 (2014) 13748-13754.

[40] K. Asakura, X-ray absorption fine structure for Catalysts and Surfaces, in: Y. Iwasawa (Ed.) Analysis of XAFS, World Scientific, Singapore, 1996, pp. 35-58.

[41] T. Rurigaki, A. Hitotsuyanagi, M. Nakamura, N. Sakai, N. Hoshi, Structural effects on the oxygen reduction reaction on the high index planes of Pt3Ni: n(111)–(111) and n(111)–(100) surfaces, J. Electroanal. Chem., 716 (2014) 58-62.

[42] J. Perez, E.R. Gonzalez, H.M. Villullas, Hydrogen Evolution Reaction on Gold Single-Crystal Electrodes in Acid Solutions, J. Phys. Chem. B, 102 (1998) 10931-10935.

[43] C.M. Pedersen, M. Escudero-Escribano, A. Velázquez-Palenzuela, L.H. Christensen, I. Chorkendorff, I.E.L. Stephens, Benchmarking Pt-based electrocatalysts for low temperature fuel cell reactions with the rotating disk electrode: oxygen reduction and hydrogen oxidation in the presence of CO, Electrochim. Acta, 179 (2015) 647-657.

[44] J. Roques, A.B. Anderson, Cobalt concentration effect in Pt1−xCox on the reversible potential for forming OHads from H2Oads in acid solution, Surf. Sci., 581 (2005) 105-117.

[45] Y. Xiong, H. Shan, Z. Zhou, Y. Yan, W. Chen, Y. Yang, Y. Liu, H. Tian, J. Wu, H. Zhang, D. Yang, Tuning Surface Structure and Strain in Pd–Pt Core–Shell Nanocrystals for Enhanced Electrocatalytic Oxygen Reduction, Small, 13 (2017) 16034231-16034238.

[46] S. Kaneko, R. Myochi, S. Takahashi, N. Todoroki, T. Wadayama, T. Tanabe,

Ultrahigh Vacuum Synthesis of Strain-Controlled Model Pt(111)-Shell Layers: Surface Strain and Oxygen Reduction Reaction Activity, J. Phys. Chem. Lett., 8 (2017) 5360-5365.

[47] S.W. Lee, S. Chen, J. Suntivich, K. Sasaki, R.R. Adzic, Y. Shao-Horn, Role of Surface Steps of Pt Nanoparticles on the Electrochemical Activity for Oxygen Reduction, J. Phys. Chem. Lett., 1 (2010) 1316-1320.

[48] B.E. Conway, Electrochemical oxide film formation at noble metals as a surface-chemical process, Prog. Surf. Sci., 49 (1995) 331-452.

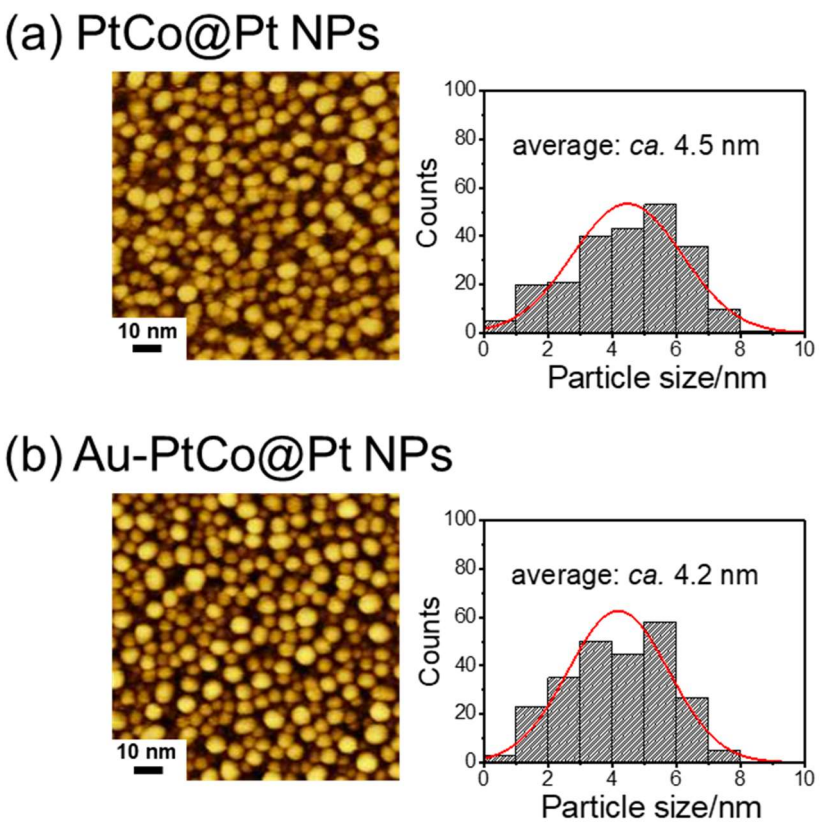

Fig. 1. STM images and particle size distribution histograms for PtCo@Pt (a) and Au-PtCo@Pt (b).

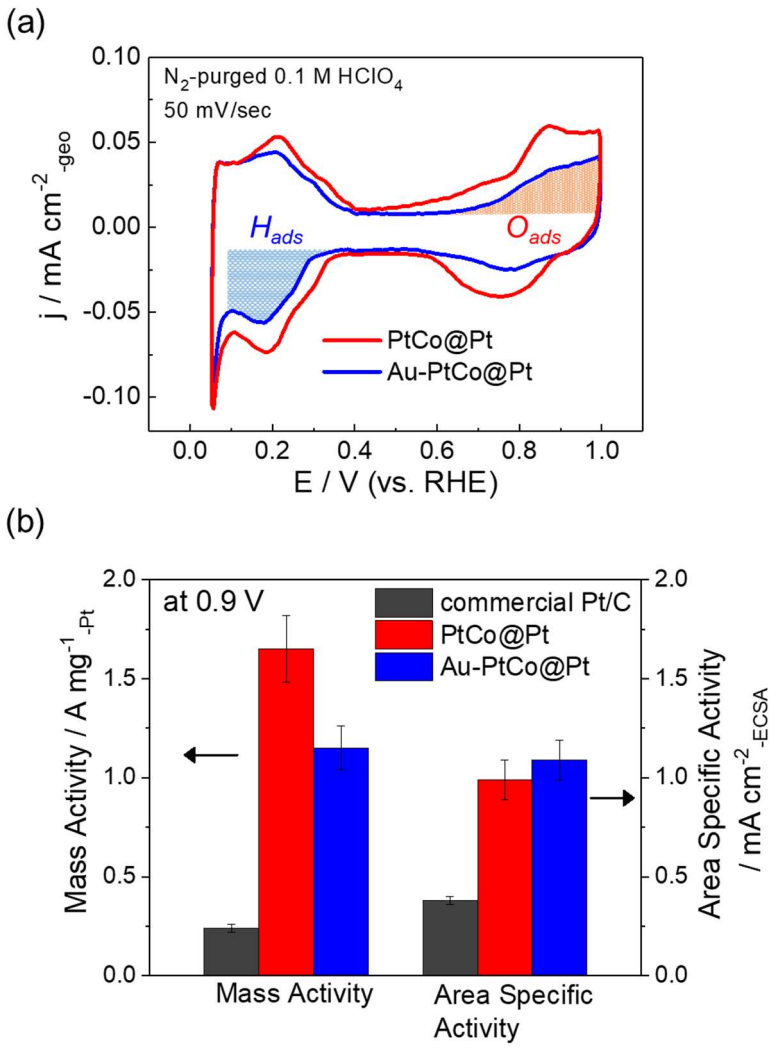

Fig. 2. (a) Cyclic voltammograms of PtCo@Pt and Au-PtCo@Pt samples recorded in N_2-purged 0.1 M $HClO_4$. (b) Initial mass activity and area-specific activity at 0.9 V of PtCo@Pt and Au-PtCo@Pt samples. Recently reported values[10,43] for commercial Pt/C catalysts are also added.

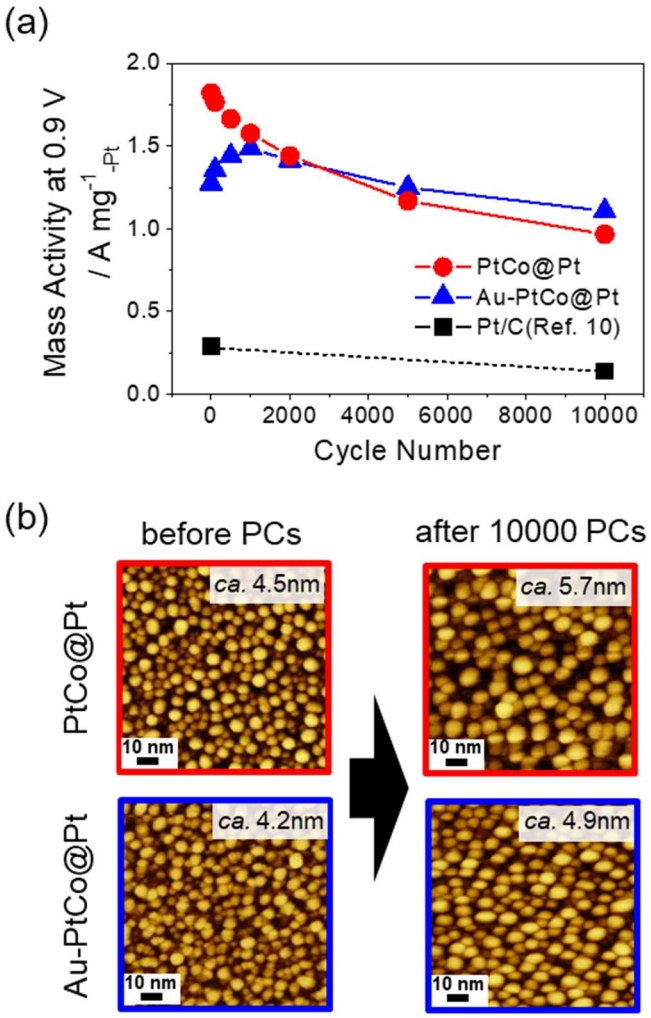

Fig. 3. (a) Mass activity changes in PtCo@Pt (red) and Au-PtCo@Pt (blue) samples as a function of the number of potential cycles when applying PCs between 0.6 and 1.0 V (ADT). The reported value[10] for a commercial Pt/C catalyst is also added. (b) STM images collected before (initial) and after 10,000 PCs.

Table 1. Summary of EXAFS curve fitting results of Pt L_3 edge for Pt, PtCo@Pt, and Au-PtCo@Pt NPs recorded in N_2-purged 0.1 M $HClO_4$ at 0.4 V vs. RHE.

Sample	Bond	N^a	R (nm)^b	σ^2 (10^{-2}nm^2)^c	R-factor (%)^d
Pt	Pt-Pt	9.8 ± 1.0	2.75 ± 0.01	0.54 ± 0.10	1.5
PtCo@Pt	Pt-Pt	7.7 ± 0.7	2.74 ± 0.01	0.50 ± 0.00	1.9
	Pt-Co	2.1 ± 0.8	2.66 ± 0.03	1.20 ± 0.00	
Au-PtCo@Pt	Pt-Pt	6.9 ± 2.2	2.74 ± 0.01	0.41 ± 0.19	2.6
	Pt-Co	3.8 ± 2.5	2.67 ± 0.01	1.43 ± 0.93	

[a]*N* is the coordination number. [b]*R* is the bond distance. [c]σ^2 is the Debye-Waller factor. [d]*R-factor* is the fitting quality (residual).

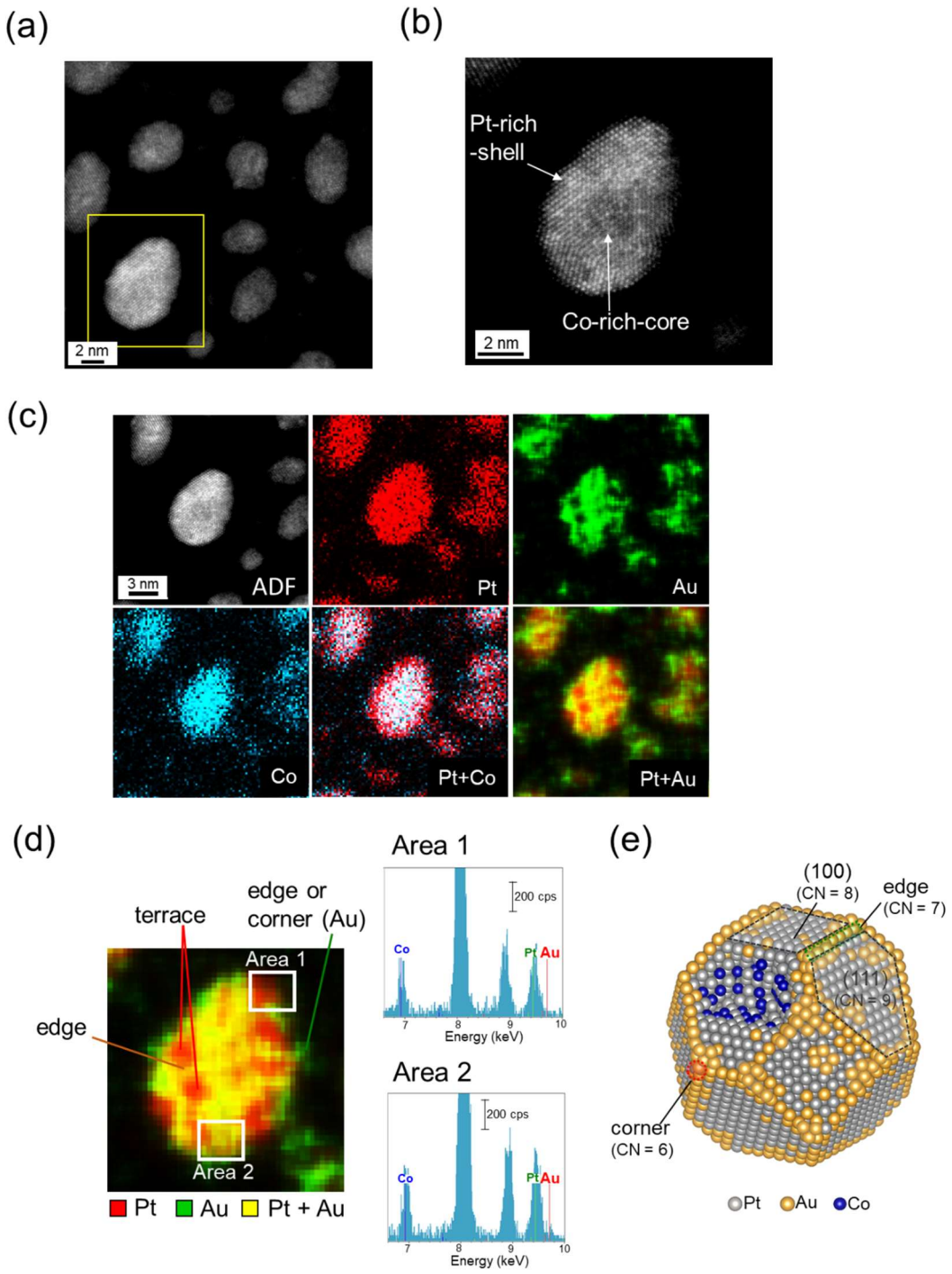

Fig. 4. (a) HAADF-STEM image of Au-PtCo@Pt. (b) Magnified image of the region inside the yellow square in (a). (c) STEM-EDS elemental mapping of Au-PtCo@Pt NPs; the maps of Au and "Pt+Au" are smoothed to clarify the images using the ESPRIT software. (d) left: magnified STEM-EDS image of "Pt+Au"; right: corresponding energy dispersive spectra for Areas 1 (top) and 2 (bottom) of the STEM-EDS image in the region from 6.5 to 10 keV. (e) Cuboctahedral structural model of the Au-PtCo@Pt NP.